A Mock Data Challenge for the Einstein Gravitational-Wave Telescope

Tania Regimbau,[1, a] Thomas Dent,[2, b] Walter Del Pozzo,[3] Stefanos Giampanis,[4] Tjonnie G.F. Li,[3] Craig Robinson,[2, 5] Chris Van Den Broeck,[3] Duncan Meacher,[2] Carl Rodriguez,[2] B.S. Sathyaprakash,[2] and Katarzyna Wójcik[2]

[1] *UMR ARTEMIS, CNRS, University of Nice Sophia-Antipolis, Observatoire de la Côte d'Azur, BP 4229, 06304, Nice Cedex 4, France*
[2] *School of Physics and Astronomy, Cardiff University, 5 The Parade, Cardiff, CF24 3AA, UK*
[3] *Nikhef – National Institute for Subatomic Physics, Science Park 105, 1098 XG Amsterdam, The Netherlands*
[4] *University of Wisconsin-Milwaukee P.O. Box 413, 2200 E. Kenwood Blvd. Milwaukee, WI 53201-0413, USA*
[5] *Maryland Center for Fundamental Physics, Department of Physics, University of Maryland, College Park, MD 20742, USA*

Einstein Telescope (ET) is conceived to be a third generation gravitational-wave observatory. Its amplitude sensitivity would be a factor ten better than advanced LIGO and Virgo and it could also extend the low-frequency sensitivity down to 1–3 Hz, compared to the 10–20 Hz of advanced detectors. Such an observatory will have the potential to observe a variety of different GW sources, including compact binary systems at cosmological distances. ET's expected reach for binary neutron star (BNS) coalescences is out to redshift $z \simeq 2$ and the rate of detectable BNS coalescences could be as high as one every few tens or hundreds of seconds, each lasting up to several days. With such a signal-rich environment, a key question in data analysis is whether overlapping signals can be discriminated. In this paper we simulate the GW signals from a cosmological population of BNS and ask the following questions: Does this population create a confusion background that limits ET's ability to detect foreground sources? How efficient are current algorithms in discriminating overlapping BNS signals? Is it possible to discern the presence of a population of signals in the data by cross-correlating data from different detectors in the ET observatory? We find that algorithms currently used to analyze LIGO and Virgo data are already powerful enough to detect the sources expected in ET, but new algorithms are required to fully exploit ET data.

PACS numbers:

I. INTRODUCTION

After a decade of detector installation and commissioning, ground-based detectors looking for gravitational waves (GWs) have reached or surpassed their design sensitivities and are poised to open up a new window onto the Universe, as well as allowing coincident searches with electromagnetic or neutrino detectors. The first generation of interferometric observatories (GEO [1], LIGO [2] and Virgo [3]) have already put interesting constraints, for example, on the ellipticity of the Crab pulsar [4] and on the cosmological stochastic background [5]. With the second generation starting in a few years, one expects to detect compact binary coalescences in the local Universe [6], while third generation detectors, such as the Einstein Telescope [7], should take GW astronomy to a new level, due to the large numbers of high SNRs of detectable sources, making it possible to address a range of problems on a wide variety of astrophysical sources but also in fundamental physics and cosmology.

The coalescence of two neutron stars (BNS), two black holes (BBH) or a neutron star and a black hole (NS-BH), are the most promising sources for terrestrial detectors, due to the huge amount of energy emitted in the last phase of their inspiral trajectory, merger, and ringdown. The maximum distance probed with current detectors is about 30 Mpc [8] for BNS, but the next generation of detectors should be taking data with a sensitivity approximately 10 times greater, pushing the horizon up to about 450 Mpc [6]. With the third generation Einstein Telescope, the sensitivity will be increased by another order of magnitude and the horizon of compact binaries is expected to reach cosmological distances [9]. Among other things, this will allow for a detailed study of the evolution of binary coalescences over redshift [10], measurement of the mass function of neutron stars and black holes and of the neutron star equation of state [11, 12], and the use of binary neutron stars and neutron star-black hole binaries as standard sirens to constrain dark energy and its time evolution [13–15] (for a summary of ET science objectives see Ref. [9]). In such a large volume, however, the number of sources can be as large as a million and the waveforms may overlap to create a confusion foreground, especially at low frequencies where the signal can last for several days [17]. This could affect our ability to make individual detections and perform parameter estimation, and the issue deserves thorough study.

With this in mind, we have simulated Einstein Telescope detector noise and added signals from a population of compact binaries, with a view to issuing a Mock Data Challenge (MDC) to the gravitational-wave community. This could be used to develop advanced data analysis methods in order to separate the sources and measure the properties of both individual sources and of

[a] Electronic address: Tania.Regimbau@oca.eu
http://www.oca.eu/regimbau/ET-MDC˙web/ET-MDC.html
[b] Electronic address: Thomas.Dent@astro.cf.ac.uk

the catalog as a whole. Initially we used a simple BNS inspiral signal model, but work is in progress to include other types of sources and more sophisticated scenarios. In the longer term we envisage issuing *ET science challenges* to encompass not only detection of signals and parameter estimation, but also the application of such results to outstanding problems in fundamental physics, astrophysics and cosmology.

In Section 2, we present the Einstein Telescope; in Section 3 we describe our procedure to simulate the mock data; in Section 4 we present the results of the search for both individual sources and the integrated signal; in Section 5 we discuss future developments for the mock data and in the search methods; finally in Section 6 we draw our conclusions.

II. EINSTEIN TELESCOPE

A conceptual design study was recently concluded for the proposed European project, the *Einstein gravitational wave Telescope* (ET) [18]. The goal of the study was to explore the technological challenges and the scientific benefits of building a third generation gravitational wave detector that is a factor 10 better than advanced detectors but also capable of observing at frequencies down to 1–3 Hz [7]. In this Section we will discuss the optical configuration of ET, different design choices for its sensitivity and ET's response to gravitational waves and its distance reach to compact binary coalescences.

A. Optical topology and sensitivity

Consideration of many factors including continuous observation (duty cycle), ability to resolve the two polarizations of GW, and capacity to support new designs over many decades, led to the conclusion that the infrastructures housing the current detectors will be inadequate to meet the design goals of ET. The Einstein Telescope is envisioned to consist of three V-shaped Michelson interferometers with 60 degree opening angles, arranged in a triangle configuration (see Fig. 1, left panel). These are to be placed underground to reduce the influence of seismic noise.

The design goal to push the sensitivity floor at low frequency down to 1–3 Hz comes from the requirement that ET be sensitive to more massive coalescing binaries than advanced detectors, *i.e.* intermediate mass BBH of masses in the range 10^2–$10^4\,M_\odot$ [19–22], but also be able to observe stellar mass binaries for far longer periods before they merge. With better low-frequency sensitivity, the subtle secular general-relativistic effects that occur in strong gravitational fields will accumulate over longer periods[1], facilitating a deeper understanding of GW sources, and in addition allowing the source's redshift to be measured, in the case of binaries where one or both components is a neutron star [15][2].

It is highly challenging, and perhaps technically unfeasible, to push the low frequency limit down to 1–3 Hz in a single interferometer while still achieving a broad-band improvement of an order of magnitude in sensitivity over Advanced detectors [23]. The technology that achieves better high frequency ($\gtrsim 100$ Hz) sensitivity, *i.e.* higher laser power to bring down the photon shot noise, is in direct conflict with that required to improve low frequency ($\lesssim 100$ Hz) sensitivity, *i.e.* lower thermal noise and radiation pressure noise, since these are both worsened by higher laser power. One of the designs considered by the design study team is the so-called *xylophone* configuration [24]. The idea is to install two interferometers in each V of the triangle, one that has good high-frequency sensitivity and the other with good low-frequency sensitivity [24, 25]. Several other new technologies, for instance frequency-dependent squeezing of light, have been studied in detail for the ET design [18] and must be combined to achieve the sensitivity goals of third generation detectors [26].

With 10 km arm lengths, 500 W of input laser and 3 MW of arm cavity power for the high frequency interferometer, and 3 W of input laser and 18 kW of arm cavity power and the use of cryogenic technology (mirrors cooled to 10 K), for the low frequency interferometer [18, 25], ET's sensitivity is expected to be about a factor of 10 better than that of advanced detectors, allowing for the detection of sources at cosmological distances, while also achieving good sensitivity in the 3–10 Hz region. Fig. 1, right panel, compares the sensitivity of a xylophone configuration (ET-D) [25] with that of a single interferometer (ET-B) [23]. Also plotted for comparison are the design sensitivity curves of advanced LIGO (zero-detuned high-power) [27] and Virgo [28] (labelled aLIGO and aVirgo), initial LIGO [29] and Virgo [30].

B. Response function and antenna pattern

Let us begin by looking at ET's response to GW signals. Far away from a source, gravitational waves emitted by a system can be expressed in a suitable coordinate system as a transverse and symmetric trace-free (STF) tensor h^{ij} (all temporal components of the metric perturbation vanish) whose only non-zero spatial components

[1] For instance, a reduction by a factor of 4 in the low frequency cutoff increases the duration of a binary source in band by a factor of 40.

[2] In [15] a lower frequency cutoff of 10 Hz was used; if this cutoff is reduced to 3 Hz, the errors on recovered redshift are reduced by tens of percent, up to nearly a factor 2 improvement for sources at redshift 4 [16].

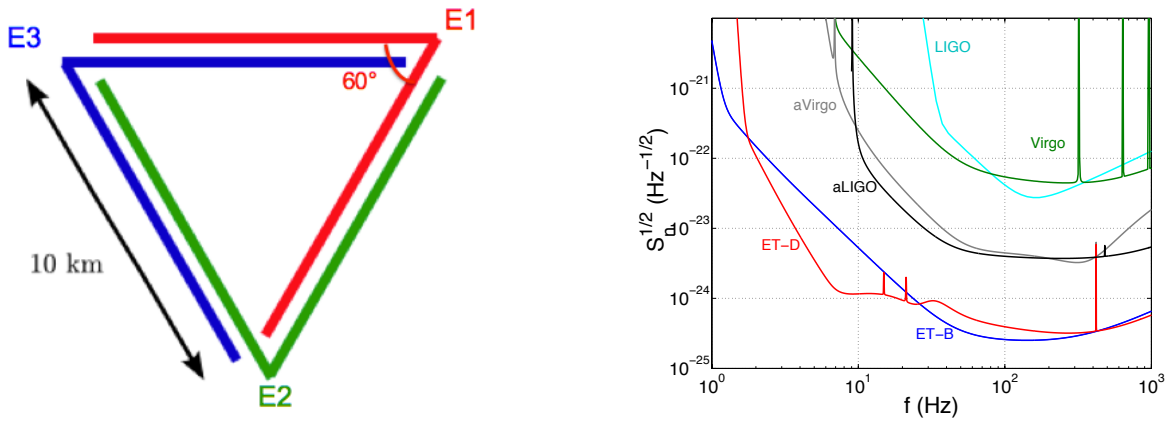

FIG. 1: Left : Configuration of the planned detector Einstein Telescope. Right : design sensitivity of two possible configurations (ET-B and ET-D) compared to the sensitivity of first generation detectors (here LIGO and Virgo) and the projected sensitivity of second generation (advanced) detectors (here the aLIGO zero-detuned high-power noise curve [27] and aVirgo [28]).

are

$$h^{11} = -h^{22} = h_+, \quad h^{12} = h^{21} = h_\times. \tag{1}$$

Let $(\mathbf{e}_x, \mathbf{e}_y, \mathbf{e}_z)$ be an orthonormal triad in which the metric perturbation takes the transverse-traceless form. Then, using basis polarization tensors defined as

$$\mathbf{e}_+ \equiv \mathbf{e}_x \otimes \mathbf{e}_x - \mathbf{e}_y \otimes \mathbf{e}_y, \quad \mathbf{e}_\times \equiv \mathbf{e}_x \otimes \mathbf{e}_y + \mathbf{e}_y \otimes \mathbf{e}_x, \tag{2}$$

the metric perturbation can be written as

$$\mathbf{h} = h_+ \, \mathbf{e}_+ + h_\times \, \mathbf{e}_\times. \tag{3}$$

ET's interferometers can also be represented as STF tensors:

$$\begin{aligned} \mathbf{d}^1 &= \frac{1}{2}(\mathbf{e}_1 \otimes \mathbf{e}_1 - \mathbf{e}_2 \otimes \mathbf{e}_2), \\ \mathbf{d}^2 &= \frac{1}{2}(\mathbf{e}_2 \otimes \mathbf{e}_2 - \mathbf{e}_3 \otimes \mathbf{e}_3), \\ \mathbf{d}^3 &= \frac{1}{2}(\mathbf{e}_3 \otimes \mathbf{e}_3 - \mathbf{e}_1 \otimes \mathbf{e}_1), \end{aligned} \tag{4}$$

where $\mathbf{e}_1$, $\mathbf{e}_2$ and $\mathbf{e}_3$ are unit vectors along the three arms of ET. The response $h^A(t)$, $A = 1, 2, 3$, of the interferometers to an incident gravitational wave is just the inner product of the detector tensor $\mathbf{d}^A$ with the wave tensor $\mathbf{h}$:

$$h^A(t) = d^A_{ij} \, h^{ij} = d^A_{ij} e^{ij}_+ \, h_+ + d^A_{ij} e^{ij}_\times \, h_\times, \tag{5}$$

which motivates definition of the antenna pattern functions F^A_+ and $F^A_\times$:

$$F^A_+ \equiv d^A_{ij} \, e^{ij}_+, \quad F^A_\times \equiv d^A_{ij} \, e^{ij}_\times, \tag{6}$$

in terms of which the response can be written as

$$h^A(t) = d^A_{ij} \, h^{ij} = F^A_+ \, h_+ + F^A_\times \, h_\times. \tag{7}$$

Let us now choose a coordinate system fixed to ET such that the three arms of ET's triangle are in the xy-plane and the unit vectors along the arms are

$$\begin{aligned} \mathbf{e}_1 &= \frac{1}{2}\left(\sqrt{3}, \ -1, \ 0\right), \quad \mathbf{e}_2 = \frac{1}{2}\left(\sqrt{3}, \ 1, \ 0\right), \\ \mathbf{e}_3 &= \left(0, \ 1, \ 0\right). \end{aligned} \tag{8}$$

Let (θ, φ) be the direction to the source in this coordinate system with $(\mathbf{e}_\theta, \mathbf{e}_\theta)$ denoting directions of increasing θ and φ, respectively.

The unit vectors $\mathbf{e}_x$, $\mathbf{e}_y$ and $\mathbf{e}_z$ defining the radiation frame can be obtained by successive counterclockwise rotations about the z-axis by an angle φ, about the new y-axis by an angle θ and the final z-axis by an angle ψ:

$$\begin{aligned} \mathbf{e}_x &= (-\sin\varphi \, \sin\psi + \cos\theta \, \cos\varphi \, \cos\psi, \ \cos\varphi \, \sin\psi + \cos\theta \, \sin\varphi \, \cos\psi, \ -\sin\theta \, \cos\psi), \\ \mathbf{e}_y &= (-\sin\varphi \, \cos\psi - \cos\theta \, \cos\varphi \, \sin\psi, \ \cos\varphi \, \cos\psi - \cos\theta \, \sin\varphi \, \sin\psi, \ -\sin\theta \, \sin\psi), \\ \mathbf{e}_z &= (\sin\theta \, \cos\varphi, \ \sin\theta \, \sin\varphi, \ \cos\theta), \end{aligned}$$

where ψ is the polarization angle defined by $\cos\psi = \mathbf{e}_\theta \cdot \mathbf{e}_x$. The antenna pattern functions of the interferometer whose arms are $(\mathbf{e}_1, \mathbf{e}_2)$ is:

$$F^1_+ = -\frac{\sqrt{3}}{4}\big[(1+\cos^2\theta)\,\sin 2\varphi\,\cos 2\psi + 2\,\cos\theta\,\cos 2\varphi\,\sin 2\psi\big], \tag{9}$$

$$F^1_\times = +\frac{\sqrt{3}}{4}\big[(1+\cos^2\theta)\,\sin 2\varphi\,\sin 2\psi - 2\,\cos\theta\,\cos 2\varphi\,\cos 2\psi\big]. \tag{10}$$

The antenna pattern functions are a factor $\sin\gamma = \sqrt{3}/2$ smaller than that of an L-shaped detector of the same length, where $\gamma = \pi/3$ is the opening angle of ET's interferometer arms.

The antenna pattern functions of the other two detectors in ET, with arms $(\mathbf{e}_2, \mathbf{e}_3)$ and $(\mathbf{e}_3, \mathbf{e}_1)$, are obtained from F^1_+ and $F^1_\times$ by the transformation $\varphi \to \varphi \pm 2\pi/3$:

$$F^2_{+,\times}(\theta,\varphi,\psi) = F^1_{+,\times}(\theta,\varphi+2\pi/3,\psi), \tag{11}$$

$$F^3_{+,\times}(\theta,\varphi,\psi) = F^1_{+,\times}(\theta,\varphi-2\pi/3,\psi). \tag{12}$$

F^A_+ and $F^A_\times$ are sometimes called antenna *amplitude* pattern functions to distinguish them from their squares $(F^A_+)^2$ and $(F^A_\times)^2$, which are called antenna *power* pattern functions [31]. The overall response of an interferometer to an incident wave depends on the square root of the sum of the antenna power pattern functions $F^2_+ + F^2_\times$. The joint response of all the three detectors in the ET network is

$$F^2 = \sum_{A=1}^{3} (F^A_+)^2 + (F^A_\times)^2, \tag{13}$$

which can be shown to be equal to

$$F^2 = \frac{9}{32}\left(1 + 6\cos^2\theta + \cos^4\theta\right). \tag{14}$$

Thus, the joint antenna power pattern depends only on the colatitude θ of the source. ET's response is smaller compared to an L-shaped interferometer by a factor $\sqrt{3}/2$ due to the 60° opening angle, but its 3 detectors enhance its response by $\sqrt{3}$, leading to an overall factor of 3/2. This is indeed what we find: $F(0) = 3/2$. The response averaged over θ is $\sqrt{\langle F^2\rangle} = \sqrt{2/5}\,F(0) \simeq 0.63\,F(0)$ and its minimum value is $F(\pi/2) = F(0)/\sqrt{8} \simeq 0.35\,F(0)$. With an average response 63% of its optimum and a worst response 35% of its optimum, and with no null directions, ET has virtually all-sky coverage.

C. Null stream

It follows immediately from Eqs. (4), (5) that the sum of the individual responses $\sum_A h^A$ is identically equal to zero. The sum of the responses of any set of Michelson interferometers forming a closed path is zero and is called the *null stream*. As we shall discuss later, such a null stream is an invaluable tool in data analysis.

Two L-shaped detectors with arm lengths of 7.5 km (and total length of 30 km), rotated relative to each other by an angle $\pi/4$, are completely equivalent to ET in terms of their response and resolvability of polarizations. However, their response cannot be used to construct a null stream.

D. Distance reach to compact binaries

In 1986 Schutz showed [59] that inspiralling binary systems are standard candles whose (luminosity) distance can be measured from the observed gravitational wave signal, without the need to calibrate sources at different distances. Our detectors are able to measure both the apparent and absolute luminosity of the radiation, and hence to extract the luminosity distance of such a source: the magnitude of the gravitational wave strain gives the apparent luminosity but the rate at which the signal's frequency changes gives the absolute luminosity.

For simplicity we shall consider a binary that is located at an optimal position on the sky (overhead with respect to the plane of ET) and optimally oriented (i.e. its angular momentum is along the line of sight). The discussion below holds good even when these assumptions are dropped, but the measurement of the various angular parameters would be essential in order to disentangle the distance. This would require a network of three or more detectors with long baselines to triangulate the source's position on the sky. We will also only consider the GW quadrupole amplitude in this discussion; higher-order corrections to the amplitude do not affect the conclusions.

The magnitude of the strain measured by our detectors when the signal frequency reaches the value f is

$$h = \frac{4\mathcal{M}}{D}\,[\pi\mathcal{M}f(t)]^{2/3}\,\cos\left[\int_0^t f(t')\,\mathrm{d}t'\right], \tag{15}$$

where $\mathcal{M}$ is the chirp mass of the binary, related to its total mass $M = m_1 + m_2$ and symmetric mass ratio $\nu = m_1 m_2/M^2$ by $\mathcal{M} = \nu^{3/5}M$, and D is the proper distance to the source. Note that this expression is valid in the limit of asymptotically flat, static spacetime; we will soon discuss the effect of cosmological expansion on the observed signal.

In addition to the signal's strain we can also measure

the rate at which its frequency changes[3] via

$$\frac{df}{dt} = \frac{96\,\mathcal{M}^{5/3}}{5\pi}\,(\pi f)^{11/3} \;\Rightarrow\; \mathcal{M} = \left(\frac{5\pi\,\dot{f}}{96}\right)^{3/5} (\pi f)^{-11/5}. \tag{16}$$

Thus, measurement of the signal strain and rate of change of frequency can together determine the system's chirp mass and its distance from Earth.

For cosmological sources, however, the distance recovered by this method is not the comoving distance to the source χ (equivalent to D for a spatially flat FRW universe), but rather its luminosity distance $D_{\rm L} = (1+z)\chi$. This may be explained as follows: due to time dilation, the chirp mass of the system inferred from Eq. (16) will be "redshifted" by a factor $(1+z)$, thus the signal will appear to have come from a source whose chirp mass is $(1+z)\mathcal{M}$. Thus, if we reconstruct the masses of the binary from the frequency evolution of the waveform, we will obtain redshifted masses a factor $(1+z)$ larger than the physical masses of the system at redshift z. Symbols such as m, M, $\mathcal{M}$ will denote physical masses, whereas when discussing "redshifted" observed mass parameters we will use a superscript z, for instance $m_1^z \equiv (1+z)m_1$.

This increase in apparent mass does not, however, mean that we will observe a greater signal amplitude: gravitational-wave amplitude, being dimensionless, cannot change due to redshift. Given this, and noting that $\mathcal{M}f$ is invariant under the effect of redshift, we find that a source with physical chirp mass $\mathcal{M}$ will appear to us to have a chirp mass $(1+z)\mathcal{M}$, and its apparent distance will be the luminosity distance $D_{\rm L} = (1+z)\chi$, instead of the proper or comoving distance.

Let us now consider the distance reach of ET to an inspiral signal from a compact binary of component masses m_1 and m_2, at a luminosity distance $D_{\rm L}$ and whose orbit (assumed here to be quasi-circular) makes an angle ι with the line of sight. There exist different measures of the distance reach of a detector: the *horizon distance* is commonly used in data analysis (see, for instance, [32]), while *detector range* and *range functions* were defined by Finn and Chernoff [33] and are routinely used as a measure of detector performance. Our measures of distance reach are inspired by all of these concepts.

The signal-to-noise ratio (SNR) ρ_A for a given signal (such as from an inspiralling binary), detected by matched filtering with an optimum filter, in a detector labelled A, is

$$\rho_A^2 = 4\int_0^\infty \frac{|H_A(f)|^2}{S_n(f)}\,{\rm d}f, \tag{17}$$

where $H_A(f)$ is the Fourier transform of the response of detector A and $S_n(f)$ is the one-sided noise power spectral density (PSD) of the detector, which we assume to be the same for all three detectors in the ET array. A good analytical fit [34] to the ET-B noise PSD is given by $S_n(f) = 10^{-50} h_n(f)^2\,{\rm Hz}^{-1}$, where

$$\begin{aligned} h_n(f) &= 2.39\times10^{-27}\,x^{-15.64} + 0.349\,x^{-2.145} \\ &+ 1.76\,x^{-0.12} + 0.409\,x^{1.10}, \end{aligned} \tag{18}$$

and where $x = f/100\,{\rm Hz}$. We may write the detector response in terms of two GW polarizations via $H_A(f) = F_+^A H_+ + F_\times^A H_\times$, where

$$H_+(f) = \sqrt{\frac{5}{24}}\,\frac{(G\mathcal{M}^z)^{5/6}}{\pi^{2/3}c^{3/2}D_{\rm L}}\,\frac{(1+\cos^2\iota)}{2}\,f^{-7/6}, \tag{19}$$

$$H_\times(f) = \sqrt{\frac{5}{24}}\,\frac{(G\mathcal{M}^z)^{5/6}}{\pi^{2/3}c^{3/2}D_{\rm L}}\,\cos\iota\,f^{-7/6}. \tag{20}$$

The coherent SNR ρ for the ET network is simply the quadrature sum of the individual SNRs: $\rho^2 = \sum \rho_A^2$. For low mass systems such as BNS, the SNR is dominated by the inspiral part of the signal; the coherent SNR can then be shown to reduce to

$$\rho^2 = \frac{5}{6}\,\frac{(G\mathcal{M}^z)^{5/3}\mathcal{F}^2}{c^3\pi^{4/3}\,D_{\rm L}^2}\int_{f_1}^{f_2}\frac{f^{-7/3}}{S_n(f)}\,{\rm d}f, \tag{21}$$

where f_1 and f_2 are lower and upper frequency cutoffs chosen so that the integral has negligible (say, $< 1\%$) contribution outside this range and $\mathcal{F}$ is a function of all the angles given by

$$\mathcal{F}^2 \equiv \sum_A \left[\frac{1}{4}(1+\cos^2\iota)^2\,(F_+^A)^2 + \cos^2\iota\,(F_\times^A)^2\right]. \tag{22}$$

Here $F_{+\,\times}^A$, $A = 1, 2, 3$, are the antenna pattern functions of the detector given by Eqs. (9)-(12). Substituting for the antenna pattern functions and summing over the three detectors gives

$$\begin{aligned} \mathcal{F}^2(\theta,\,\varphi,\,\psi,\,\iota) &= \frac{9}{128}\left(1+\cos^2\iota\right)^2\left(1+\cos^2\theta\right)^2\cos^2 2\psi \\ &+ \frac{9}{32}\left(1+\cos^2\iota\right)^2\cos^2\theta\sin^2 2\psi \\ &+ \frac{9}{32}\cos^2\iota\left(1+\cos^2\theta\right)^2\sin^2 2\psi \\ &+ \frac{9}{8}\cos^2\iota\cos^2\theta\cos^2 2\psi. \end{aligned} \tag{23}$$

The quantity $\mathcal{F}$ determines the SNR of a source of a given (observed) chirp mass at any given distance. Although the antenna power pattern F^2 is independent of $(\varphi,\,\psi)$, the quantity $\mathcal{F}$ is only independent of φ. For certain source locations and orientations, the response is still independent of the polarization angle. For instance, either when the source is "overhead" with respect to ET's plane (*i.e.* $\theta = 0, \pi$) or face-on (*i.e.* $\iota = 0, \pi$), $\mathcal{F}$ is independent of ψ. It depends weakly on ψ for values of θ and

[3] In reality we don't directly measure the evolution of the frequency but use matched filtering to dig out the signal buried in noisy data. The end result, however, is the same. In fact, post-Newtonian approximation has allowed the computation of very accurate signal models which allows us to infer not only the chirp mass but also the mass ratio of the system.

ι significantly different from these extreme values. The maximum value $\mathcal{F}_{\rm max} = 3/2$ is obtained when $\theta = \iota = 0$, while the value of $\mathcal{F}^2$ averaged over $(\theta,\, \psi,\, \iota)$ is

$$\overline{\mathcal{F}^2} = \frac{1}{8\pi}\int_0^{\pi}\int_0^{\pi}\int_0^{2\pi} \mathcal{F}^2 \,\sin\theta\,\sin\iota\,\mathrm{d}\theta\,\mathrm{d}\iota\,\mathrm{d}\psi = \frac{9}{25}.$$

So the root-mean-square value of $\mathcal{F}$ is $\mathcal{F}_{\rm rms} \equiv \sqrt{\overline{\mathcal{F}^2}} = 3/5$. The *horizon distance* $\hat{D}_{\rm L}$ of a detector is defined as the maximal distance at which an optimally oriented, overhead binary (*i.e.* $\iota = \theta = 0$) can be detected above a threshold SNR of $\rho = \rho_T$, chosen large enough to keep the false alarm rate acceptably low; $\rho_T = 8$ is considered reasonable for current detectors. Noting that $\mathcal{F} = 3/2$ when $\iota = \theta = 0$, for ET the horizon is given by

$$\hat{D}_{\rm L} \equiv \sqrt{\frac{15}{8}}\,\frac{(G\mathcal{M}^z)^{5/6}}{\pi^{2/3}c^{3/2}\,\rho_T}\left[\int_{f_1}^{f_2}\frac{f^{-7/3}}{S_h(f)}\,\mathrm{d}f\right]^{1/2}. \qquad (24)$$

The horizon distance is not a very useful measure since essentially no signals can be detected beyond this distance with an SNR larger than ρ_T. A more meaningful measure of the reach is the distance $\overline{D}_{\rm L}$ at which an "average" source, meaning one for which $\mathcal{F} = \mathcal{F}_{\rm rms} = 3/5$, produces an SNR of ρ_T. For such a source we obtain

$$\overline{D}_{\rm L} = \frac{3}{5}\,\hat{D}_{\rm L}. \qquad (25)$$

For a binary consisting of two components of (physical) mass $1.4\,M_\odot$ and for a threshold $\rho_{\rm T} = 8$, we find $\overline{D}_{\rm L} \simeq 13\,$Gpc or $z = 1.8$, and $\hat{D}_{\rm L} \simeq 37\,$Gpc or $z = 4$, but it can be larger for more massive binaries. In our simulations, we inject signals of different orientations and polarization angles distributed uniformly over comoving volume up to a redshift of $z = 6$.

E. Efficiency vs. distance

The *efficiency* of a detector at a given distance, and for binary sources with given physical component masses, is the fraction of such sources for which ET achieves an expected SNR $\rho \geq \rho_T$. ET will not be sensitive to every BNS merger at any given distance, but only to those that are preferentially located in certain sky directions and are suitably oriented [33]. The fraction $\epsilon(D_{\rm L})$ of sources detected by ET at a given luminosity distance is given by

$$\epsilon(D_{\rm L}) = \frac{1}{8\pi}\int_0^{\pi}\int_0^{\pi}\int_0^{2\pi} \Pi(\rho/\rho_T - 1)\,\sin\theta\,\sin\iota\,\mathrm{d}\theta\,\mathrm{d}\iota\,\mathrm{d}\psi, \qquad (26)$$

where Π is the unit step function $\Pi(x) = 0$ if $x < 0$ and $\Pi(x) = 1$ if $x > 0$. Note that ρ is a function of all angles, luminosity distance, redshift, etc. In Figure 7, top right, we plot ET's efficiency as a function of redshift for binary neutron stars: the blue solid curve shows the efficiency for physical masses $m_1 = m_2 = 1.4\,M_\odot$, choosing a SNR threshold $\rho_T = 8$ and a lower frequency cutoff $f_1 = 1\,$Hz. As shown in this figure, ET should have 50% efficiency at a redshift of $z \sim 1.3$, while its efficiency at $z = 1.8$ (distance at which the angle-averaged SNR is 8) is 30%.

III. SIMULATION OF ET MOCK DATA

In this section we will discuss how ET mock data was generated. We will describe the cosmological model used and the rate of coalescence of binary neutron stars as a function of redshift. We will also discuss how the background noise was generated and the waveform model used in the simulation.

A. Simulation of the GW Signal

We use Monte Carlo techniques to generate simulated extra-galactic populations of binary neutron stars and produce time series of the gravitational wave signal in the frequency band of ET. We first describe how the distribution of injected BNS sources over redshift and mass was obtained, and then explain the simulation pipeline summarized in Fig. 3.

We first consider the rate of BNS coalescences in the Universe. We neglect the possible production of compact binaries through interactions in dense star systems, and we assume that the final merger of a compact binary occurs after two massive stars in a binary system have collapsed to form neutron stars and have inspiralled through the emission of gravitational waves. The merger rate tracks the star formation rate, albeit with some delay t_d from formation of the binary to final merger.

Following [17], we write the coalescence rate density $\dot{\rho}_c(z)$ (in $\mathrm{Mpc}^{-3}\,\mathrm{yr}^{-1}$) as:

$$\dot{\rho}_c(z) \propto \int_{t_d^{\rm min}}^{\infty} \frac{\dot{\rho}_*(z_f(z,t_d))}{1+z_f(z,t_d)} P(t_d)\,\mathrm{d}t_d \;\text{ with }\; \dot{\rho}_c(0) = \dot{\rho}_0\,, \qquad (27)$$

where $\dot{\rho}_*$ is the star formation rate of [36] (in $\mathrm{M}_\odot\,\mathrm{Mpc}^{-3}\,\mathrm{yr}^{-1}$), z the redshift when the binary system merges, z_f the redshift when the binary system is formed, $P(t_d)$ the probability distribution of the delay connecting z and z_f, and $\dot{\rho}_0$ the rate density in our local universe. The normalization condition reproduces the local rate density for $z = 0$ and the factor $(1+z_f)^{-1}$ converts the rate density in the source frame into a rate density in the observer frame.

The redshifts z_f and z are related by the *delay time* t_d which is the sum of the time from the initial binary formation to its evolution into a compact binary, plus the merging time τ_m after which emission of gravitational waves occurs. The delay is also the difference in lookback times between z_f and z:

$$t_d = \frac{1}{H_0}\int_z^{z_f} \frac{\mathrm{d}z'}{(1+z')E(\Omega,z')}\,. \qquad (28)$$

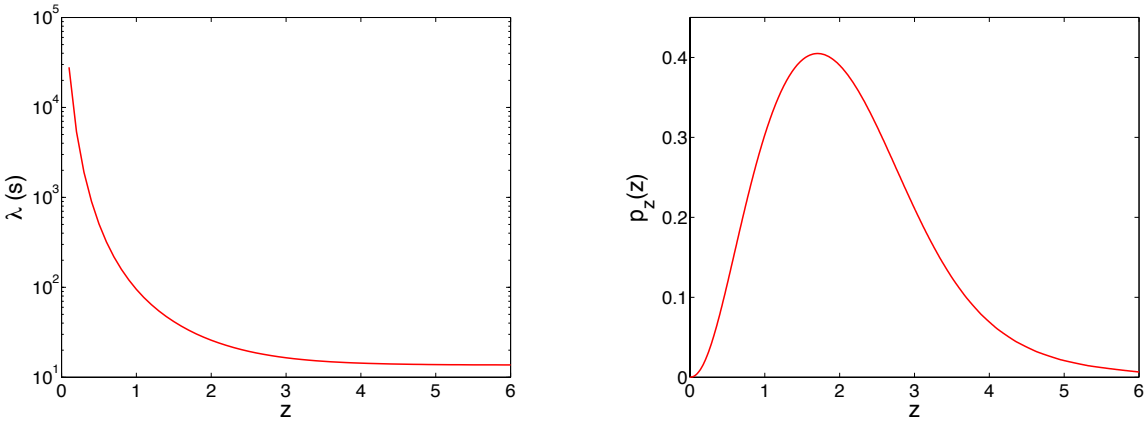

FIG. 2: Left: Average waiting time as a function of maximal redshift. Right: Probability distribution of the redshift, assuming the star formation rate of [36], a distribution of the delay of the form $P(t_d) \propto 1/t_d$ with minimal delay of 20 Myr and a local coalescence rate density of 1 Mpc^{-3} Myr^{-1}.

where

$$E(\Omega, z) = \sqrt{\Omega_\Lambda + \Omega_m (1+z)^3}\,. \tag{29}$$

In these simulations, we have assumed a flat Universe with $\Omega_m = 0.3$ and $\Omega_\Lambda = 0.7$ and Hubble parameter $H_0 = 70\,\mathrm{km\ s^{-1}\,Mpc^{-1}}$.

We assume a distribution of the form $P(t_d) \propto 1/t_d$, as suggested by population synthesis [37], with a minimal delay $t_d^{\min} = 20\,\mathrm{Myr}$, corresponding roughly to the time it takes for massive binaries to evolve into two neutron stars [38]. This broad model accounts for the wide range of merger times observed in binary pulsars; it is also consistent with short gamma ray burst observations in both late and early type galaxies [39].

The coalescence rate per redshift bin is then is given by

$$\frac{dR}{dz}(z) = \dot\rho_c(z) \frac{dV}{dz}\,, \tag{30}$$

where dV/dz is the comoving volume element:

$$\frac{dV}{dz}(z) = 4\pi \frac{c}{H_0} \frac{r(z)^2}{E(\Omega, z)}\,, \tag{31}$$

where

$$r(z) = \frac{c}{H_0} \int_0^z \frac{\mathrm{d}z'}{E(\Omega, z')}\,, \tag{32}$$

is the proper distance.

The average waiting time $\overline{\Delta t}$ between signals is calculated by taking the inverse of the coalescence rate, Eq. (30), integrated over all redshifts:

$$\lambda = \left[\int_0^{z_{\max}} \frac{dR}{dz}(z)\,\mathrm{d}z \right]^{-1}. \tag{33}$$

Fig. 2, left panel, shows Δt as a function of the maximal redshift $z_{\max}$ out to which which events are injected, given a local coalescence rate of $\dot\rho_0 = 1\,\mathrm{Myr^{-1}\,Mpc^{-3}}$ which corresponds to the galactic rate estimated in [35], and which we adopt here.

We assume that signals arrive at the detector as a Poisson process and draw the time intervals $\Delta t = t_c^{j+1} - t_c^j$ between successive coalescences at times t_c^{j+1} and t_c^j, from an exponential distribution $P(\Delta t) = \exp(-\Delta t/\lambda)$. Coalescence times t_c^k are generated between the start time of the observation t_i and the end time t_f, to which we add the maximal duration $\tau_{\max}$ that a source can have in our frequency range (a $1.2 + 1.2\,\mathrm{M}_\odot$ system at $z = 0$).

Then, we proceed as follows for each source:

1. The physical masses of the two neutron stars are drawn from a Gaussian distribution with mean $1.4\,M_\odot$ and variance $0.5\,M_\odot$, and are restricted to the interval $[1.2, 3]\,M_\odot$.

2. The redshift is drawn from a probability distribution $p(z)$ obtained by normalizing the coalescence rate dR/dz in the interval 0–$z_{\max}$:

$$p_z(z) = \lambda \frac{dR}{dz}(z)\,. \tag{34}$$

   Next we calculate the duration of the waveform in our frequency range:

$$\tau \sim 5.4\,\mathrm{day} \left(\frac{\mathcal{M}^z}{1.22 M_\odot} \right)^{-5/3} f_1^{-8/3}\,, \tag{35}$$

   where f_1 is the low-frequency cutoff of the detector.

3. For each source visible in our observation time-window $[t_i, t_f]$, the source's location in the sky, its

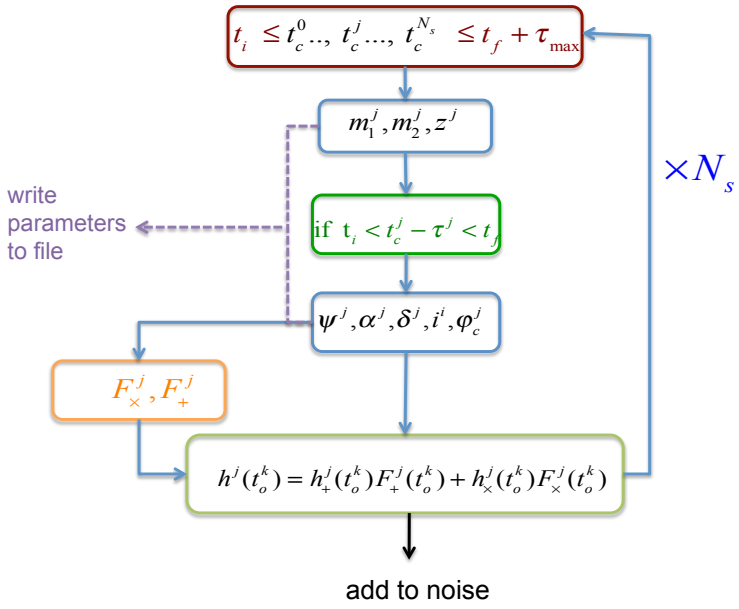

FIG. 3: Flow diagram of the Monte Carlo simulation code

orientation, the polarization angle and the phase at the coalescence are drawn from uniform distributions.

4. The gravitational wave signal $h(t) = F_+(t)h_+(t) + F_\times h_\times(t)$ of the source is calculated for each detector E1, E2 and E3 and for each observation time t_o^k until the frequency reaches f_1, and is added to the time series. In these simulations, we have used so-called TaylorT4 waveforms [44], up to 3.5 post-Newtonian order in phase $\phi(t)$ and only the most dominant lowest post-Newtonian order term in amplitude:

$$h_+(t) = A(t)(1+\cos^2\iota)\cos[\phi(t)] \quad (36)$$
$$h_\times(t) = 2A(t)\cos\iota\cos[\phi(t)] \quad (37)$$

where ι, as before, is the inclination angle of the binary with respect to the line of sight.

The signal amplitude is then

$$A(t) \sim 2\times10^{-21}\left(\frac{1\,\mathrm{Mpc}}{D_\mathrm{L}}\right)\left(\frac{\mathcal{M}^z}{1.2\,M_\odot}\right)^{5/3}\left(\frac{f(t)}{100\,\mathrm{Hz}}\right)^{2/3},$$

where the luminosity distance D_L is in Mpc, $\mathcal{M}^z$ in $\mathrm{M}_\odot$, and where $f(t)$ in Hz is the instantaneous gravitational-wave frequency (twice the binary's orbital frequency) which increases monotonically as the system shrinks and gets closer to merger. For a description of the TaylorT4 approximant and how it relates to other waveform approximants, see [45] and references therein.

An example time series of the gravitational wave signal including sources up to a redshift $z \sim 6$ is shown in the top plot of Fig. 4, left panel. The bottom plot, left panel, shows the corresponding time domain filter, i.e., the inverse Fourier transform of the frequency-domain signal weighted by the noise power spectral density. This shows that, even though the *signals* will have considerable overlap, the same is not true of the filters; consequently it will be possible to resolve individual sources.

B. Simulation of the noise

In order to produce the data set, it is necessary to use a model of the expected noise for the ET detectors. To this end, we assume that the noise will be stationary and Gaussian. Moreover, for the time being, we assume that the noise realizations in the different detectors are uncorrelated. The noise for each detector was generated using the following procedure: Firstly, we generate a Gaussian time series with a mean of zero, and unit variance. These time series are Fourier transformed and coloured by the relevant ET sensitivity curve in the frequency domain. To get the final time-domain representation of the noise, we apply an inverse Fourier transform.

The noise curve used is based on the analytic fit of Eq. (18) to the ET-B PSD discussed in Section II. To alleviate the effects of possible discontinuities across frame files, the PSD is gradually tapered to zero below the low frequency limit $f_l = 10\,\mathrm{Hz}$, and above a frequency of $f_2 \equiv f_\mathrm{Nyquist}/2$. Fig. 4, right panel, shows the noise curve used to colour the data, with the tapering applied,

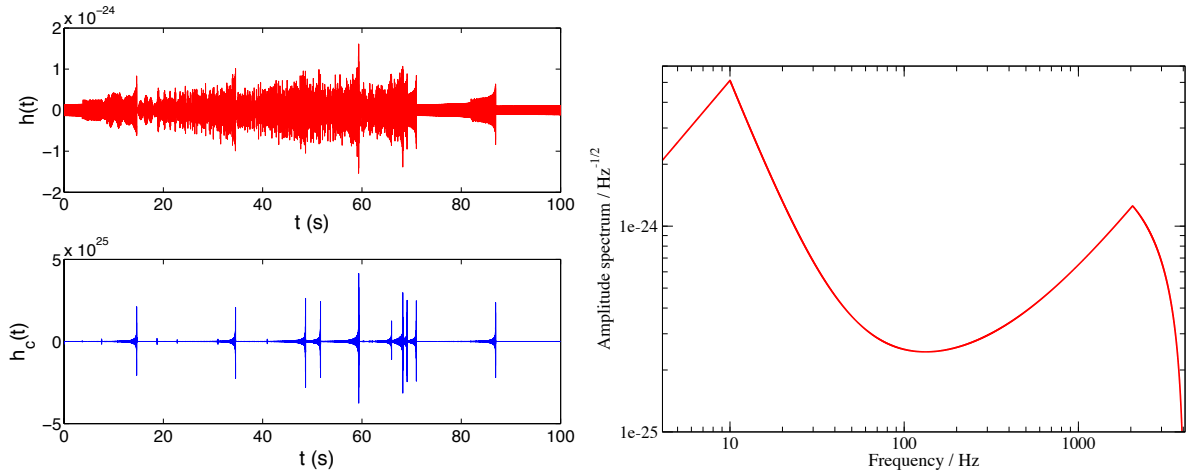

FIG. 4: Left: Simulated time series of the gravitational strain at detector E1, for $z_{\rm max} = 6$ and $f_1 = 10\,$Hz (top) and the same time series after the Fourier transform has been divided by the noise power spectral density of ET. Right: The tapered projected ET noise spectrum used to color the noise. Example audio files of the simulated GW signal alone or in the presence of noise can be found at the ET MDC website `http://www.oca.eu/regimbau/ET-MDC_web/ET-MDC.html`.

for a sample rate of 8192 Hz.

IV. FIRST ANALYSIS

A. Null stream

A *null stream* is a combination of the detector output streams such that the gravitational wave signal is identically zero and only noise remains. The existence of an ET null stream was noted already in [46] and is a major motivation for the triangular triple Michelson topology. Given an incident GW tensor h_{ij}, the three interferometer responses were derived in Eq. 5, from which, as already remarked in Section II C, we find that the sum of the three detector responses to any GW signal vanishes identically. We may define the *null stream* as the sum of the strain time series $x(t)$ for the three ET detectors. For each single detector A we have

$$x^A(t) \equiv n^A(t) + d^A_{ij} h^{ij}(t), \tag{38}$$

where $n^A(t)$ is the noise realization, thus

$$\begin{aligned} x_{\rm null}(t) &\equiv \sum_{A=1}^{3} x^A(t) \\ &= \sum_{A=1}^{3} n^A(t) + \sum_{I=1}^{3} d^A_{ij} h^{ij}(t) \\ &= \sum_{A=1}^{3} n^A(t) \end{aligned} \tag{39}$$

is free of GW signals, and will also not contain any common (correlated) noise for which the sum over the three detectors happens to vanish.

If the noise properties are homogeneous among the detectors,

$$S_n^1(f) \simeq S_n^2(f) \simeq S_n^3(f)\,, \tag{40}$$

and if correlations between detectors can be neglected, we can use the null stream to estimate the average PSD in each of the three detectors. In this case,

$$\begin{aligned} \langle X_{\rm null}(f) X^*_{\rm null}(f')\rangle &= \left\langle \sum_{A,B} N^A N^{B*} \right\rangle \\ &\simeq \left\langle \sum_{A} N^A N^{A*} \right\rangle \\ &\simeq 3\frac{1}{2}\delta(f-f')\hat{S}_n^A(f), \end{aligned} \tag{41}$$

where $X_{\rm null}(f)$ is the Fourier transform of $x_{\rm null}(t)$ and, in the last line, $\hat{S}_n^A(f)$ is the noise PSD in any of the three interferometers *in the absence of a GW signal*. Defining

$$\langle X_{\rm null}(f) X^*_{\rm null}(f')\rangle = \frac{1}{2}\delta(f-f') S_{n,{\rm null}}(f), \tag{42}$$

we find

$$\hat{S}_n^A(f) \simeq \frac{1}{3} S_{n,{\rm null}}(f) \tag{43}$$

as an estimate for the individual single-interferometer PSDs with the signals removed.

The null stream PSD, which we plot on the left panel of Fig. 5, then has the advantage of giving a better representation of the noise content of the three detectors. The typical sensitivity improvement is nonetheless fairly small, about 1% in the 10 – 100 Hz band. As a proof

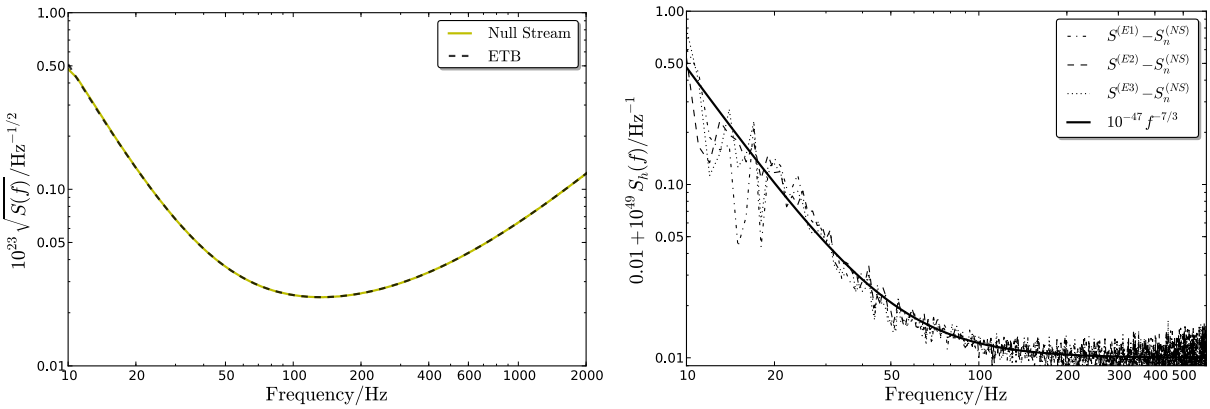

FIG. 5: *Left*—Sample PSD calculated from the null stream, compared to the theoretical ETB fit 18. The null PSD is estimated within data segments of length 2048 s by averaging non-overlapping samples each of 1 s length, and is then averaged over all 2048 s long segments in the dataset. The figure shows $\sqrt{S_{n,\mathrm{null}}(f)/3}$. *Right*—Difference between (one-third of) the null stream PSD and the E_j PSDs obtained by averaging over the whole dataset, as defined in Eq. 44. The residuals are consistent with the $f^{-7/3}$ spectrum expected from binary inspiral signals. To aid visibility, the quantities plotted have been scaled by 10^{49} and the constant 0.01 has been added.

of principle of the effectiveness of the use of null stream PSD instead of the single detector one, we computed the median over the whole dataset of the difference between (one-third of) the null stream PSD and the individual detector PSD's $S_n^A(f)$. These residuals should be consistent with the median PSD of the injected signals in each detector:

$$S_n^A(f) - \frac{1}{3}S_{n,\mathrm{null}} \simeq \hat{H}(f) \tag{44}$$

where $\hat{H}(f)$ is the power spectral density of GW signals. The result of this operation is shown in Fig. 5, right panel. The residual spectrum between 10 and 400 Hz in each detector is consistent with the theoretical expectation $S_h(f) \sim f^{-7/3}$.

B. Compact Binary Coalescence analysis

We analysed the triple coincident simulated data using a modified version of the LIGO-Virgo Ihope pipeline [8, 32, 40, 41] which is used to search for signals from compact binary coalescences (CBC). The stages of the pipeline are as follows:

- Estimation of the PSD by median over several overlapping time chunks within a 2048 s segment
- Generation of a template bank covering the chosen parameter space of binary masses
- Matched filtering of each template against the data stream of each detector to generate an SNR time series $\rho(t)$
- Trigger generation: for each template, maxima of SNR over a sliding time window of length 15 s were found, and a "trigger" was generated if any such maxima exceeded an SNR of 5.5
- Clustering to reduce trigger numbers: if there are multiple triggers within a small region of parameter space (binary masses plus time [47]) the trigger with largest SNR is selected and others in the region are discarded
- Coincidence between detectors: only pairs or triples of triggers with consistent coalescence times and masses [48] survive and are designated as events
- Ranking of events by combined SNR^2, ρ_C^2 (sum of ρ^2 over coincident triggers).

There are several differences compared to the standard LIGO-Virgo search. The main ones concern the frequency range of data searched, the parameter space of the search and the method for determining the significance of candidate events.

The length of an inspiral template increases rapidly with the lowest frequency that is matched filtered in the analysis. For technical reasons related to memory load and PSD estimation the standard matched filter code used for LSC-Virgo analyses [40] cannot filter templates longer than a few minutes: hence we chose to impose a lower frequency cutoff of 25 Hz. This limitation should be addressed in future analyses (and may be relevant to analysis of Advanced LIGO/Virgo data).

The template bank was chosen to cover the possible range of redshifted (*i.e.* observed) mass pairs corresponding to the BNS injections up to redshift 4. The minimum component mass was taken as $1.2\,M_\odot$; with a maximum injected component mass of $3\,M_\odot$, the observed total mass at $z = 4$ is then $15\,M_\odot$, which we took as

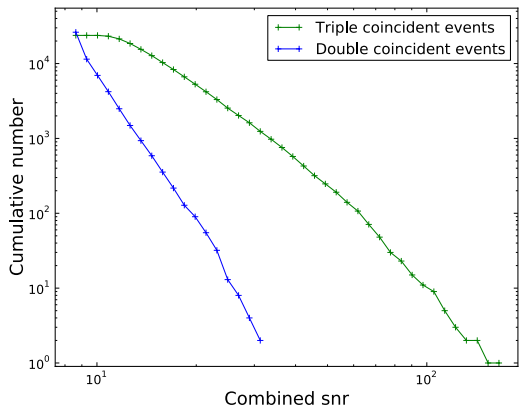

FIG. 6: Cumulative histogram of CBC events as a function of combined SNR ρ_C, divided into double (two-detector) and triple (three-detector) coincidences.

our maximum component mass, with a maximum total mass of $30\,M_\odot$. The maximum injected mass ratio is $3/1.2 = 2.5$ corresponding to a "symmetric mass ratio" $\eta = m_1 m_2/(m_1+m_2)^2 \simeq 0.204$, thus templates with $\eta < 0.2$ were removed, considerably reducing the size of the bank.

Since the simulated noise was Gaussian, signal-based vetoes and data quality vetoes were not necessary to suppress detector artefacts, and events were ranked simply by the quadrature sum of SNR over coincident triggers. The noise background in our mock data is expected to be a function of combined SNR alone, thus we set a threshold in the value of ρ_C above which we consider an event likely to be a true GW signal.

Note that the time shift method used to estimate background event rates in LIGO-Virgo searches fails here. In order for such methods to be valid, the number of detectable GW events over the search time should be small (of order 1): otherwise, loud triggers due to true GW signals may significantly distort the background distribution, by forming random time-shifted coincidences with noise triggers. In the present case we see tens of thousands of detectable signals, thus the distribution of loud time-shifted coincidences is totally dominated by such 'signal-plus-noise' events.

1. *Events found by CBC analysis*

The CBC analysis outputs a list of loudest events with the coalescence time, combined SNR, and the component masses of the best-fitting template for each event. The distribution over ρ_C is plotted in Figure 6 for both double- and triple-coincident events. Given the single-detector SNR threshold $\rho_t = 5.5$, the quietest possible double coincidence has $\rho_C = \sqrt{2}\rho_t \simeq 7.78$ and the quietest triple has $\rho_C = \sqrt{3}\rho_t \simeq 9.53$. The expected (cumulative) distribution of events from an astrophysical population is approximately proportional to the inverse cube of combined SNR (thus to the cube of the luminosity distance, or to the volume of space seen by the search). Deviations from this inverse-cube behaviour will arise due to evolution of the source population over redshift, also because the physical volume of space is no longer exactly proportional to distance^3 at large z, and also since the observed masses of a coalescing binary are larger than the physical masses by a factor $(1+z)$, changing the expected SNRs.

Over most of the range of ρ_C the distribution of triple coincidences is close to $\sim \rho_C^{-3}$ as expected; with decreasing combined SNR values, an increasing fraction of signals are seen as double coincidences. We see no significant background distribution of triples, which would be expected to rise exponentially at small combined SNR. Thus in principle the efficiency of the search could be improved by lowering the SNR threshold for triple coincidences.

The distribution of double coincidences shows two components: an approximate power-law at higher ρ_C and a more rapidly rising component below about $\rho_C = 9$. We interpret these as a cosmological population of sources, modulated by the variation in the proportion found as doubles vs. triples; and a Gaussian noise background, respectively. Thus we expect that above a combined SNR $\rho_C \gtrsim 9$ the great majority of events will be caused by binary coalescence signals rather than random noise.

2. *Efficiency and accuracy*

We evaluate the search efficiency as a function of redshift by testing time coincidence between simulated signals and found events (using a "coalescence time" at which the chirping signal reaches a well-defined frequency) and choose a time window of ± 30 ms. For a given event or injection there are the following cases:

- False event: an event which does not fall within 30 ms of an injection
- True event: an event falling within 30 ms of one or more injections
- Missed injection: a simulated signal which does not fall within 30 ms of an event
- Found injection: an simulated signal within 30 ms of a found event. [4]

[4] Note that events are clustered over time windows of a few seconds, thus more than one event cannot be found within a 30 ms window.

However, if we have very frequent candidate events or injections, we may encounter significant numbers of *wrongly found injections*, meaning chance time coincidences between injections and noise events where the expected SNR of the injected signal is below the analysis threshold. For these we do not expect the estimated mass parameters and effective luminosity distance from the analysis pipeline to correspond to those of the simulated source; the fractional error in these parameters will be order(1). Wrongly found injections would lead us to overestimate the search efficiency and would degrade the accuracy of recovered source parameters. To minimize such effects whenever two or more simulated signals fall within ± 30 ms of an event, we consider only the injection with the lowest redshift to be found. In practice this ambiguity is found to affect only a small fraction (sub-percent) of signals.

As mentioned above, we require a threshold on ρ_C to limit the number of false events caused by noise. Here we choose to impose $\rho_C > 8.8$, finding 36774 events above this threshold in the 2419200 s of data analyzed. By comparing these with the catalogue containing 177350 simulated coalescence signals over the analysis time we find 850 false events, giving a directly estimated false alarm probability (FAP) of 2.3%. The efficiency of finding injections as a function of redshift is summarized in Figure 7, top two panels.

In the top right plot we compare the efficiency of the current analysis with the theoretical ideal efficiency defined in Eq. 26, for two different values of the threshold SNR ρ_T and the low frequency cutoff f_1. The ihope analysis does somewhat worse than the corresponding theoretical curve, which can in part be attributed to the single-detector SNR threshold $\rho_t = 5.5$; the theoretical calculation does not impose a lower limit on the amplitude of signals in single detectors contributing coherently to the significance of an event.

We evaluate the accuracy of the recovered (observed) chirp mass $\mathcal{M}^z$ via the discrepancy $(\mathcal{M}^z_{\rm rec} - \mathcal{M}^z_{\rm inj})/\mathcal{M}^z_{\rm inj}$ plotted in Figure 7, lower left plot.[5] The vast majority of events found have a well recovered chirp mass with an accuracy better than 0.5%, even for the small number of sources recovered at redshift $z > 4$: the number of wrongly found injections with violently inaccurate $\mathcal{M}$ is order(10). The chirp mass is the chief parameter governing the frequency evolution of a compact binary system due to its emission of energy in GW, thus we can deduce the luminosity in GW of such systems with good accuracy out to extremely large distances. But note again that we cannot determine the system's *physical* masses without an independent determination of its redshift.

[5] Note that the fractional error in observed chirp mass $\mathcal{M}^z$ is mathematically identical to the fractional error in physical chirp mass $\mathcal{M}$.

The distribution of errors in observed total mass M^z is significantly broader: see Figure 7, lower right plot, where there is a slight overall bias towards overestimating M^z and a small population of injections for which the total mass is overestimated by 5–10%. We find that this population consists of nearly equal-mass binaries which are found with somewhat more asymmetrical templates. Since the inspiral signal is significantly less sensitive to changes in mass ratio or total mass keeping a fixed $\mathcal{M}$ than vice versa, we expect a larger spread in recovered M values than in $\mathcal{M}$. We may also expect a bias in the recovered mass parameters due to taking the maximum SNR value over the template bank, since the density of templates (and thus the probability of an upward SNR fluctuation) is greater at smaller $\mathcal{M}$ and at smaller η.

C. Stochastic

The superposition of the GW signals from our population of BNS create a background which is expected to be isotropic (the source position in the sky and polarization were selected from a uniform distribution) and stationary (the length of the data is much greater than the time interval between successive events, and the duration of the waveform). Its properties in the frequency domain can be characterized by the dimensionless energy density parameter [42]:

$$\Omega_{gw}(f) = \frac{1}{\rho_{cr}} \frac{d\rho_{gw}}{d\ln f}, \tag{45}$$

where $\rho_{\rm gw}$ is the gravitational energy density and $\rho_{cr} = 3c^2 H_0^2/(8\pi G)$ the critical energy density needed to make the Universe flat today.

This quantity is related to the one-sided ($f > 0$) power spectral density in gravitational waves, at the detector output (S_h) :

$$\Omega_{gw}(f) = \frac{10\pi^2}{3\sin^2(\gamma) H_0^2} f^3 S_h(f) \tag{46}$$

where γ is the opening angle of the interferometer arms.

Note that the background from BNS is not Gaussian at frequencies > 10 Hz, in the sense that the number of sources overlapping at a given time is too small for the central limit theorem to apply and for the distribution of the sum of the amplitudes to have a Gaussian distribution. Thus, knowledge of $\Omega_{gw}(f)$ does not *completely* specify the statistical properties of the background, as there may be non-vanishing moments other than the variance. In particular, the amplitude distribution of the GW signal may exhibit large tails compared to the Gaussian case.

For the population of neutron stars distributed according to the probability distributions discussed in Sec.III.A for the mass, redshift, position in the sky, polarization and inclination, the predicted Ω_{gw} is shown in Fig. 8,

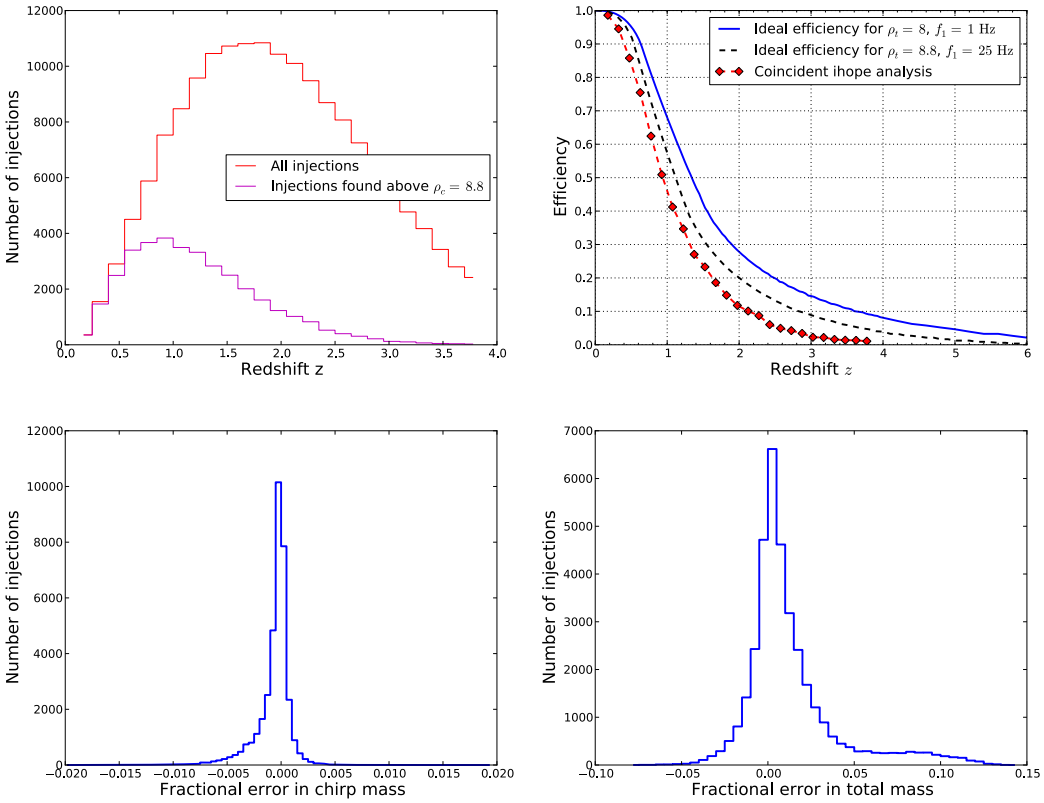

FIG. 7: *Top left*—Distributions of all BNS injections, and those found by the CBC pipeline, vs. redshift. Here events with $\rho_C > 8.8$ were considered as candidate signals. *Top right*—Efficiency of the CBC search vs. redshift. We show the theoretical (ideal) efficiency as defined in Eq. 26 for a threshold SNR of $\rho_T = 8$ and a low frequency cutoff $f_1 = 1\,\mathrm{Hz}$, and also for $\rho_T = 8.8$, $f_1 = 25\,\mathrm{Hz}$ for comparison with the signals found by the ihope pipeline. *Bottom left*—Histogram of fractional errors in chirp mass. *Bottom right*—Histogram of fractional errors in total mass.

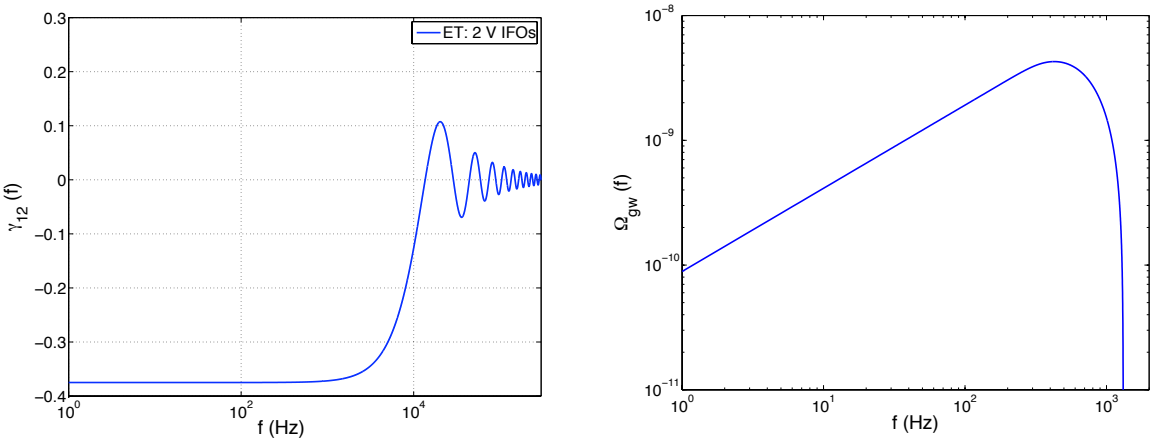

FIG. 8: *Left*—Overlap reduction function for two V-shaped ET detectors separated by 120 degrees. *Right*—Energy density parameter of the background produced by the coalescence of binary neutron stars, as a function of observed frequency.

right panel, and can be derived from the expression [49–51]:

$$\Omega_{gw}(f) = \frac{1}{\rho_{cr} c} f F(f) \tag{47}$$

where the integrated flux at the observed frequency f is given by the sum of all the individual contributions at all redshifts:

$$F(f) = \int_0^{z_{\max}} \frac{\mathrm{d}z}{4\pi D_{\mathrm{L}}^2(z)} \frac{dE_{gw}}{df}(f, \bar{\mathcal{M}}(1+z)) \frac{dR}{dz}(z) \tag{48}$$

where D_{L} is the luminosity distance, $\frac{dE_{gw}}{df}$ the spectral energy density averaged over orientation and $\bar{\mathcal{M}}$ is the average physical chirp mass of the population.

In the quadrupolar approximation, and assuming a circular orbit,

$$\frac{dE_{gw}}{df}(f, \mathcal{M}^z) = \frac{(G\pi)^{2/3} (\mathcal{M}^z)^{5/3}}{3} f^{-1/3}, \text{ for } f < f^z_{lso} \tag{49}$$

where $f^z_{lso} = (1+z)^{-1} f_{lso}$ is the observed (redshifted) frequency at the last stable orbit. The predicted energy density parameter increases as $f^{2/3}$ before it reaches a maximum $\Omega_{gw} \sim 4 \times 10^{-9}$ at around 600 Hz, with a reference value at 100 Hz of $\Omega_{\mathrm{ref}} = 1.9 \times 10^{-9}$.

The strategy to search for a Gaussian (or continuous) background, which could be confused with the intrinsic noise of a single interferometer, is to cross-correlate measurements of multiple detectors. When the background is assumed to be isotropic, unpolarized and stationary, the cross-correlation product is given by: [42]

$$Y = \int_0^\infty \tilde{s}_1^*(f) \tilde{Q}(f) \tilde{s}_2(f) \, \mathrm{d}f \tag{50}$$

and the expected variance, which is dominated by the noise, by

$$\sigma_Y^2 \simeq \int_0^\infty P_1(f) P_2(f) |\tilde{Q}(f)|^2 \, \mathrm{d}f, \tag{51}$$

where

$$\tilde{Q}(f) \propto \frac{\gamma_{12}(f) \Omega_{\mathrm{gw}}(f)}{f^3 P_1(f) P_2(f)} \tag{52}$$

is a filter that maximizes the signal-to-noise ratio (S/N). In the above equation, P_1 and P_2 are the one-sided power spectral noise densities of the two detectors and γ_{12} is the normalized overlap reduction function, characterizing the loss of sensitivity due to the separation and the relative orientation of the detectors: see Fig. 8), left panel. For two V-shaped detectors ($\gamma = \pi/3$) separated by $\beta = 2\pi/3$ degrees, $\gamma_{12}(0) = \sin^2(\gamma)\cos(2\beta) = -3/8$. The normalization ensures that $\gamma_{12} = 1$ for co-located and co-aligned L-shaped detectors.

We analyzed the data with the cross-correlation code developed by the LIGO stochastic group. The data were split into $N = 40320$ segments of length $T_{seg} = 60$ s, and for each segment the cross-correlation product and the theoretical variance were calculated using a template $\Omega \sim f^{2/3}$ in the range $10 - 500$ Hz. The frequency resolution of our analysis was 0.25 Hz. The final point estimate at 100 Hz is given by [52, 53]

$$\hat{\Omega} = \frac{Y_{opt}}{T_{seg} \sum_i \sigma_{Y,i}^{-2}} \tag{53}$$

where Y_i and $\sigma^2_{Y,i}$ are the cross-correlations and variances calculated for each segment via Eq. (50), (51) respectively, and Y_{opt} is the weighted sum

$$Y_{opt} = \sum_i Y_i \, \sigma_{Y,i}^{-2}. \tag{54}$$

The standard error on this estimate is given by

$$\sigma_\Omega = \left[\sum_i \sigma_{Y,i}^{-2} \right]^{-1/2} T_{seg}^{-1}. \tag{55}$$

For each of the pairs E1-E2, E2-E3 and E1-E3, we found a point estimate of 1.02×10^{-9} with error $\sigma_\Omega = 2.6 \times 10^{-11}$ at 100 Hz.

Our point estimate is about a factor of 2 smaller than the analytical expectation of 1.9×10^{-9}, for which all the sources between $z = 0 - 6$ are included. The discrepancy comes essentially from the suppression by our statistics of occasional high signal-to-noise-ratio events belonging to the *shot noise* regime where sources are separated by long stretches of silence [54]. We checked than when removing the loudest sources (with a signal-to-noise ratio > 8 for the sensitivity of ET-B) in the analytical calculation Eq. 48, the expected amplitude agreed to our point estimate within the σ_Ω error bar. We also verified that when removing the closest sources ($z < 0.2$) in both the data and the analytical calculation Eq. 48, the expected amplitude and the point estimate agreed within the σ_Ω error bar.

Methods able to probe better the low-rate regime are currently under development and will be tested in future Mock Data Challenges [79, 80]. However, even if the background from compact binaries is not a *Gaussian continuous* stochastic background, but rather a *popcorn-like* background in the considered frequency range $f > 10$ Hz [17, 51, 54], our analysis has shown that non-Gaussian regimes can still be probed by the standard cross-correlation statistics near optimal sensitivity, confirming the results of [79].

V. FUTURE DEVELOPMENT

This first set of Mock Data included only a single type of signal, although the BNS systems we simulated are expected to be the most numerous and can thus yield much interesting information for astrophysics and cosmology.

Moreover due to computational limitations we did not extend the simulations below a frequency of 10 Hz, though doing so might significantly improve the ability to extract signal parameters. Future Mock Data sets should address these and other points by:

1. Including more types of GW sources;
2. Using more complete or realistic waveforms;
3. Using a more sophisticated noise model.

Under the first heading, binary coalescence signals including stellar mass or intermediate mass black holes (IMBH) [19–22] are of particular interest. A small number of burst sources such as Type II supernovae are expected in the ET dataset and numerical simulations (for instance [55]) could be used to produce injection waveforms. It is also possible that primordial stochastic GW backgrounds exist in the ET sensitive band [18]; detecting these and determining their parameters would be an interesting challenge given the significant contribution of astrophysical sources. For BNS coalescences, our injected waveforms could be improved by extending the lower frequency cutoff, but also by modelling the merger phase (which depends strongly on the equation of state of NS matter, as well as the component masses). We expect that significant science can be extracted from BNS mergers, and from the tidal deformations occurring in the premerger phase, that are neglected in the PN waveform model we currently use [11, 12]. Finally, we can simulate more realistic noise by adding occasional random glitches to the data, which may be supposed to be of instrumental or environmental origin.

A. Challenges for CBC analysis

The initial search for coalescing binaries presented here, although moderately efficient below $z = 1$, has some significant drawbacks. Here we discuss how it could be improved, and point to some current developments in CBC data analysis.

In order to realize the full potential of ET's low frequency sensitivity down to 10 Hz and below, waveforms lasting on the order of an hour or more should be matched filtered. For this a simple template bank as used in current searches would be prohibitively computationally costly [56, 57] containing hundreds of thousands of templates or more. Currently, multi-band filter methods are being developed [58] which split up the waveform into time slices with different frequency content: thus the earlier part of the waveform can be downsampled, reducing computational load. The resulting template banks for each time slice are still large, and can be significantly reduced by singular value decomposition [60, 61] allowing a computationally realistic search to be performed, while retaining the ability to reconstruct the SNR for each of the original templates.

We saw that the sensitivity of the coincident analysis was limited by the SNR threshold applied to single-detector triggers. Due to this threshold, signals from distant sources were often seen as double coincidences, which compete with a much larger noise background rate than triples. To address this issue a *coherent* search should be performed, allowing the matched filter time series from all three detectors to contribute to the significance of a likely event [62–65]. For co-located detectors there is no fundamental difficulty in performing a coherent search.

We did not implement the null stream estimate of Eq. (43) for the single-detector PSD within the CBC analysis. The difference with respect to the individual detector PSDs, including the contribution of signals, was less than 1%, which we do not expect to cause a measurable change in efficiency; however, if the contributions of GW signals were significantly higher, it might be beneficial to use the null stream PSD for template placement and matched filtering.

To obtain an unbiased estimate of the source parameters for each signal, a Bayesian analysis of the strain data should be performed [66–69]. The chief conceptual challenge is the likely presence of *many* signals within any stretch of data longer than about a minute [17]. Naïvely, in order to model them one would have to multiply the dimensionality of the source parameter space by the number of signals, however more efficient methods should exist; the problem is analogous to one faced in identifying multiple galactic binary sources in mock LISA data [70] and [57] suggested that similar algorithms, for instance Markov Chain Monte Carlo based codes, could be used for ET. There will also be computational challenges in performing the analysis on hour-long stretches of data.

A conceptually difficult problem, not present in the current set of ET mock data, is to identify signals among an unmodelled background of non-Gaussian noise transients, when the rates of signals and transients may both be large. As seen in the initial CBC analysis, the method of background estimation via time shifts between detectors is invalid if signals are frequent. The broad sensitivity spectrum and increased length of binary coalescence signals visible in ET gives us hope that signal-based vetoes based on the distribution of power over frequency [71] will be effective in separating signals from noise transients. The SNR of true signals should be unaffected by the consistency test, while that of loud but badly-matched instrumental artefacts should be significantly "down-ranked" by signal-based vetoes. Current methods for optimizing these vetoes involve adding simulated signals to strain data which are assumed *not* to contain real signals; these must be revisited for ET, for example by using the null stream for doing simulations.

Given a "re-weighted SNR" statistic [72, 73] that down-ranks artefacts but not true signals, we expect to see an astrophysical event distribution of predictable form over this statistic, superimposed on a population of noise transients. If the noise distribution falls off rapidly

enough at high SNR values, it should be possible to separate the two populations simply by fitting the astrophysical component. The *null stream* will also be an essential tool to identify times when non-Gaussian noise is likely to produce loud false events, and to down-rank or veto such events.

B. Challenges for stochastic background analysis

According to various cosmological scenarios, we are bathed in a stochastic background of gravitational waves, memory of the first instant of the Universe, up to the limits of the Planck era and the Big Bang, and often seen as the Grail of GW astronomy. Proposed theoretical models include the amplification of vacuum fluctuations during inflation, pre-Big-Bang models, cosmic strings or phase transitions (see [18, 43]). In addition to the cosmological background (CGB), an astrophysical contribution (AGB) may have resulted from the superposition of a large number of unresolved sources since the beginning of stellar activity [49]. In the range of terrestrial detectors (up to $f \sim 1\,\mathrm{kHz}$) the AGB is expected to be dominated by the cosmological population of compact binaries, in particular BNS, and could be a noise that would mask the background of cosmological origin.

In this paper, we assume that the three ET detectors were independent and thus had no common (correlated) noise. A crucial prerequisite to searching ET data for stochastic GW will be to identify and remove environmental noise that can corrupt the result of cross-correlation analysis with co-located detectors. Relevant methods are under development for the two co-aligned and co-located LIGO Hanford detectors [75].

One of the most important future tasks will be to subtract the astrophysical contribution in order to allow detection of the primordial background. This could be done either in the frequency domain by modeling the power spectrum with high accuracy from theoretical studies, or characterizing its shape using Bayesian analysis of the data [74], or in the time domain by removing individual sources as previously discussed.

The nature of the AGB may also differ from its cosmological counterpart, which is expected to be stationary, unpolarized, gaussian and isotropic, by analogy with the cosmic microwave background. On the one hand, the distribution of galaxies up to 100 Mpc is not isotropic but strongly concentrated in the direction of the VIRGO cluster and the Great Attractor, and on the other hand, depending whether the time interval between events is short compared to the duration of a single event, the integrated signal may result in a continuous, popcorn noise or shot noise background [17].

In this paper we used the standard cross-correlation method for detection of stochastic GW background, but new techniques exist or are under development in the LIGO/Virgo community to search for non-isotropic [77, 78] or non-gaussian stochastic backgrounds [79, 80], and they will be tested in future challenges.

Finally, the astrophysical background is not only a noise but it could carry crucial information about the star formation history, the metallicity, the mass range of neutron star and black hole progenitors, their physical properties, the rate of compact binary mergers: developing methods for parameter estimation will represent another important task in future challenges.

VI. CONCLUSION

We have described the generation and first analyses of a mock data set for the proposed Einstein Telescope gravitational-wave observatory, containing a population of binary neutron star (BNS) inspiral signals at cosmological distances. Our motivation for this MDC is both for data analysis, to consider the different challenges encountered for data containing frequent and strong signals, and to emphasize *science challenges* in relating the results of data analysis to outstanding questions in fundamental physics, astrophysics and cosmology [18].

The design topology of the Einstein Telescope allows the construction of a unique null stream [46] independent of the sky position. We have demonstrated that it is possible to recover the average spectrum of the GW signals by subtracting the "pure noise" power spectral density (PSD) obtained from the null stream, from the PSD in each individual detector. The recovered "residual" PSD has a power-law character extremely close to the $f^{-7/3}$ behaviour expected for inspiraling binary systems. The residual PSD can either be used as a diagnosis tool for future Mock Data Challenges and stochastic analyses, or as a research tool complementary to a more traditional stochastic analysis.

The null stream is also expected to be a powerful tool for identifying and vetoing non-Gaussian features in the detector outputs; however, since the current set of ET mock data does not include such noise features, this use of the null stream will be a topic for future investigation.

The analysis used to detect coalescing binary signals was similar to current pipelines employed in searching LIGO-Virgo data, and was able to recover a large fraction of simulated signals at redshifts approaching unity. Some signals were recovered up to redshifts greater than 3 with good ($< 1\%$) accuracy on chirp mass (the chief parameter determining the frequency evolution of inspiral signals). Overlap between two or more signals only rarely affected the performance of the analysis; however this could become a more critical issue if the lower frequency cutoff (taken to be 25 Hz for the first CBC analysis) were reduced.

We also searched for the GW background created by the superposition of all the binary inspiral signals up to a redshift of $z \sim 6$ using the standard cross-correlation statistic, considering the frequency range $10 - 500\,\mathrm{Hz}$ where the spectrum can be well approximated by a power law $\Omega_{gw}(f) \propto f^{2/3}$. Our analysis shows that non-

Gaussian regimes can still be probed by the standard cross-correlation statistics near optimal sensitivity, confirming the work of [79]. Our point estimate at 100 Hz is a factor of two smaller than the analytical expectation; this difference can be understood to arise from the averaging performed in our analysis, which suppresses the contributions of rare, loud events to the estimated background. This could be improved in the future by using more sophisticated data analysis techniques that probe the non-Gaussian regime more deeply.

Future mock data will include a wider range of signals, encompassing CBC signals from BNS, NSBH/BBH, IMBH systems; a possible primordial stochastic background; and rare burst-like signals such as core-collapse supernovae. The challenge will be not only to detect these signals but to measure their parameters, and ultimately to extract a unique range of information about astrophysics, fundamental physics and cosmology from the data.

Information on future challenges, and on how to participate will be posted on the ET MDC website `http://www.oca.eu/regimbau/ET-MDC_web/ET-MDC.html`.

Acknowledgements

We are greatful to Andreas Friese, Stefan Hild, Harald Lueck and particularly Jolien Creighton, for a careful reading of the manuscript and useful comments. We thank the Albert Einstein Institute in Hannover, supported by the Max-Planck-Gesellschaft, for use of the Atlas high-performance computing cluster in the data generation and analysis, and Carsten Aulbert for technical advice and assistance. WDP, TGFL, and CVDB are supported by the research programme of the Foundation for Fundamental Research on Matter (FOM), which is partially supported by the Netherlands Organisation for Scientific Research (NWO). SG acknowledges support from NSF grant PHY-0970074 and UWM's Research Growth Initiative. BSS, CR and TD were funded by the Science and Technology Facilities Council (STFC) Grant No. ST/J000345/1 and European Community's Seventh Framework Programme (FP7/2007-2013) under grant agreement n 211743. CR was supported at Cardiff as a participant in an IREU program funded by NSF under the grant PHY-0649224 to the University of Florida. KW's visit to Cardiff was supported by the International Work Experience for Technical Students, UK, programme for 2010.

[1] B. Willke *et al.*, Class. Quant. Grav. **24**, S389 (2007).
[2] B. Abbott *et al.*, Rept. Prog. Phys. **72**, 076901 (2009).
[3] F. Acernese *et al.*, AIP Conf. Proc. **794**, 307 (2005)
[4] B. Abbott *et al.*, Astrophys. J. **683**, L45 (2008).
[5] B. Abbott *et al.*, Nature **460**, 990 (2009).
[6] J. Abadie *et al.* (LIGO Scientific Collaboration and Virgo Collaboration), Class. Quant. Grav. **27** 173001 (2010).
[7] M. Punturo *et al.*, Class. Quant. Grav. **27** 194002 (2010).
[8] J. Abadie *et al.* (LIGO Scientific Collaboration and Virgo Collaboration), Phys. Rev. D **82** (2010) 102001 [arXiv:1005.4655].
[9] B. Sathyaprakash, M. Abernathy *et al.*, "Scientific Potential of Einstein Telescope," Proceedings of Rencontres de Moriond (2011), *Gravitational Waves and Experimental Gravity*, March 21-27, La Thuile, Italy [arXiv:1108.1423].
[10] C. Van Den Broeck, to appear in the Proceedings of the 12th Marcel Grossman Meeting, Paris, 2009 [arXiv:1003.1386].
[11] J. S. Read, C. Markakis, M. Shibata, K. Uryu, J. D. E. Creighton and J. L. Friedman, Phys. Rev. D **79** (2009) 124033 [arXiv:0901.3258].
[12] T. Hinderer, B. D. Lackey, R. N. Lang and J. S. Read, Phys. Rev. D **81** (2010) 123016 [arXiv:0911.3535].
[13] B. S. Sathyaprakash, B. F. Schutz and C. Van Den Broeck, Class. Quant. Grav. **27** (2010) 215006 [arXiv:0906.4151].
[14] W. Zhao, C. Van Den Broeck, D. Baskaran, and T.G.F. Li, Phys. Rev. D **83**, 023005 (2011).
[15] C. Messenger and J. Read, arXiv:1107.5725.
[16] C. Messenger, private communication (2012).
[17] T. Regimbau and S. A. Hughes, Phys. Rev. D **79** 062002 (2009).
[18] M. Abernathy *et al.*, "Einstein gravitational wave Telescope: Conceptual Design Study", European Gravitational Observatory document number ET-0106A-10, `http://www.et-gw.eu/etdsdocument`.
[19] E. A. Huerta and J. R. Gair, Phys. Rev. D **83** (2011) 044020 [arXiv:1009.1985].
[20] E. A. Huerta and J. R. Gair, Phys. Rev. D **83** (2011) 044021 [arXiv:1011.0421].
[21] J. R. Gair, I. Mandel, M. C. Miller and M. Volonteri, Gen. Rel. Grav. **43** (2011) 485 [arXiv:0907.5450].
[22] P. Amaro-Seoane and L. Santamaria, Astrophys. J. **722** (2010) 1197 [arXiv:0910.0254].
[23] S. Hild *et al.*, arXiv:0810.0604v2 (2008).
[24] S. Hild *et al.*, Class. Quant. Grav. **27** (2010) 015003.
[25] S. Hild *et al.*, Class. Quant. Grav. **28** (2011) 094013.
[26] S. Hild, "Beyond the Second Generation of Laser-Interferometric Gravitational Wave Observatories," arXiv:1111.6277 [gr-qc].
[27] G. M. Harry and the LIGO Scientific Collaboration, Class. Quant. Grav. **27** (2010) 084006; Advanced LIGO Reference Design, LIGO Document M060056-v2, `https://dcc.ligo.org/cgi-bin/DocDB/ShowDocument?docid=m060056`. Advanced LIGO project URL is `https://www.advancedligo.mit.edu/`.
[28] G. Losurdo and the Advanced Virgo Team, Virgo document VIR-0042A-07 (2007), `https://tds.ego-gw.it/`

ql/?c=1900
[29] A. Abramovici *et al.*, Science **256** 325 (1992).
[30] B. Caron *et al.*, Class. Quant. Grav. **14** 1461 (1997).
[31] B. F. Schutz, Class. Quant. Grav. **28** (2011) 125023 [arXiv:1102.5421].
[32] B. P. Abbott *et al.* (LIGO Scientific Collaboration), Phys. Rev. D **79** (2009) 122001 [arXiv:0901.0302].
[33] L. S. Finn and D. F. Chernoff, Phys. Rev. D **47** (1993) 2198 [gr-qc/9301003].
[34] ET-B is one of the design sensitivity curves for Einstein Telescope [23]. An analytical fit for ET-B can be found at: `https://workarea.et-gw.eu/et/WG4-Astrophysics/base-sensitivity/`.
[35] V. Kalogera *et al.*, Astrophys. J. **614** 137 (2004).
[36] A. M. Hopkins and J. Beacom, Astrophys. J. **651** 142 (2006).
[37] T. Piran, Astrophys. J. **389**, L83 (1992); A. V. Tutukov and L. R. Yungelson, Mon. Not. R. Astron. Soc. **268**, 871 (1994); V. M. Lipunov *et al.*, Astrophys. J. **454**, 593 (1995); S. Ando, J. Cosmology and Astroparticle Phys. **06**, 007 (2004); J. A. de Freitas Pacheco, T. Regimbau, A. Spallici, and S. Vincent, Int. J. Mod. Phys. D **15**, 235 (2006); K. Belczynski *et al.*, Astrophys. J. **648**, 1110 (2006); R. O'Shaughnessy, K. Belczynski, and V. Kalogera, Astrophys. J. **675**, 566 (2008).
[38] K. Belczynski and V. Kalogera, Astrophys. J. Lett. **550**, L183 (2001); K. Belczynski *et al.*, Astrophys. J. **648**, 1110 (2006).
[39] E. Berger et al., Astrophys. J. **664**, 1000 (2006).
[40] B. Allen, W. G. Anderson, P. R. Brady, D. A. Brown and J. D. E. Creighton, arXiv:gr-qc/0509116.
[41] D. A. Brown for the LIGO Scientific Collaboration, Class. Quant. Grav. **22** (2005) S1097 [arXiv:gr-qc/0505102].
[42] B. Allen and J. D. Romano, Phys. Rev. D **59** (1999) 102001.
[43] M. Maggiore, Phys. Rept. **331** (2000) 283.
[44] A. Buonanno, Y.-b. Chen and M. Vallisneri, Phys. Rev. D **67** (2003) 104025 [gr-qc/0211087].
[45] A. Buonanno, B. Iyer, E. Ochsner, Y. Pan, and B. S. Sathyaprakash, Phys. Rev. D **80** 084042 (2009).
[46] A. Freise, S. Chelkowski, S. Hild, W. Del Pozzo, A. Perreca and A. Vecchio, Class. Quant. Grav. **26** (2009) 085012 [arXiv:0804.1036].
[47] C. Robinson, A. Sengupta and B. S. Sathyaprakash, `https://dcc.ligo.org/cgi-bin/DocDB/ShowDocument?docid=36649`.
[48] C. A. K. Robinson, B. S. Sathyaprakash and A. S. Sengupta, Phys. Rev. D **78** (2008) 062002 [arXiv:0804.4816].
[49] T. Regimbau, Res. Astron. Astrophys. **11** (2011) 369 [arXiv:1101.2762v3].
[50] X. J. Zhu, E. Howell, T. Regimbau, D. Blair and Z. H. Zhu, Astrophys. J. **739** (2011) 86 [arXiv:1104.3565].
[51] P. A. Rosado, Phys. Rev. D **84** (2011) 084004 [arXiv:1106.5795].
[52] B. Abbott *et al.* (LIGO Scientific Collaboration), Phys. Rev. D **95** (2005) 221101.
[53] B. Abbott *et al.* (LIGO Scientific Collaboration), Nature **460** (2009) 7258.
[54] D. Coward and T. Regimbau, New Astronomy Reviews **50** (2006) 461.
[55] C. D. Ott, A. Burrows, L. Dessart and E. Livne, Phys. Rev. Lett. **96** (2006) 201102; C. D. Ott *et al.*, Class. Quant. Grav. **24** (2007) 139, and Phys. Rev. Lett. **98** (2007) 261101; K. Kotake, W. Iwakami, N. Ohnishi and S. Yamada, Astrophys. J. Lett. **697** (2009) 133; A. Marek, H.-T. Janka and E. Muller, Astron. Astrophys. **496** (2009) 475.
[56] B. Abbott *et al.* (LIGO Scientific Collaboration), Phys. Rev. **D72** (2005) 082002 [gr-qc/0505042].
[57] L. Bosi and E. K. Porter, arXiv:0910:0380.
[58] K. Cannon *et al.*, arXiv:1107.2665 [astro-ph.IM].
[59] B. F. Schutz, Nature **323** (1986) 310.
[60] B. S. Sathyaprakash and B. F. Schutz, Class. Quant. Grav. **20** (2003) S209 [gr-qc/0301049].
[61] K. Cannon, C. Hanna and D. Keppel, arXiv:1101.4939.
[62] A. Pai, S. Dhurandhar and S. Bose, Phys. Rev. **D64** (2001) 042004.
[63] A. Pai, S. Bose and S. Dhurandhar, Class. Quant. Grav. **19** (2002) 1477.
[64] S. Bose, Class. Quant. Grav. **19** (2002) 1437.
[65] S. Bose, T. Dayanga, S. Ghosh and D. Talukder, Class. Quant. Grav. **28** (2011) 134009 [arXiv:1104.2650].
[66] C. Röver, R. Meyer and N. Christensen, Phys. Rev. D **75** (2007) 062004 [gr-qc/0609131].
[67] C. Röver, R. Meyer, G. M. Guidi, A. Vicere and N. Christensen, Class. Quant. Grav. **24** (2007) S607 [arXiv:0707.3962].
[68] J. Veitch and A. Vecchio, Class. Quant. Grav. **25** (2008) 184010 [arXiv:0807.4483].
[69] J. Veitch and A. Vecchio, Phys. Rev. D **81** (2010) 062003 [arXiv:0911.3820].
[70] S. Babak *et al.*, Class. Quant. Grav. **25** (2008) 184026.
[71] B. Allen, Phys. Rev. D **71** (2005) 062001.
[72] B. Abbott *et al.* (LIGO Scientific Collaboration), Phys. Rev. D **78** (2008) 042002 [arXiv:0712.2050].
[73] LIGO Scientific Collaboration and Virgo Collaboration, arXiv:1111.7314 [gr-qc].
[74] E. L. Robinson, J. D. Romano and A. Vecchio, Class. Quant. Grav. **25** (2008) 184019 [arXiv:0804.4144].
[75] N. Fotopoulos, Journal of Physics: Conference Series **122** (2008) 012032.
[76] C. J. Hogan and P. L. Bender, Phys. Rev. D (2001) **64** 062002.
[77] S. Mitra *et al.*, Phys. Rev. D **77** (2008) 042002 [arXiv:0708.2728].
[78] D. Talukder, S. Mitra and S. Bose, Phys. Rev. D **83** (2011) 063002. [arXiv:1012.4530].
[79] S. Drasco and E. E. Flanagan, Phys. Rev. D **67** (2003) 082003.
[80] L. Martellini and T. Regimbau, in preparation.